NANO LETTERS

pubs.acs.org/NanoLett Letter

Coexistence of Superconductivity and Antiferromagnetism in Topological Magnet $MnBi_2Te_4$ Films

Wei Yuan,[¶] Zi-Jie Yan,[¶] Hemian Yi, Zihao Wang, Stephen Paolini, Yi-Fan Zhao, Lingjie Zhou, Annie G. Wang, Ke Wang, Thomas Prokscha, Zaher Salman, Andreas Suter, Purnima P. Balakrishnan, Alexander J. Grutter, Laurel E. Winter, John Singleton, Moses H. W. Chan, and Cui-Zu Chang*

Cite This: *Nano Lett.* 2024, 24, 7962−7971 Read Online

ACCESS | Metrics & More | Article Recommendations | Supporting Information

ABSTRACT: The interface of two materials can harbor unexpected emergent phenomena. One example is interface-induced superconductivity. In this work, we employ molecular beam epitaxy to grow a series of heterostructures formed by stacking together two nonsuperconducting antiferromagnetic materials, an intrinsic antiferromagnetic topological insulator $MnBi_2Te_4$ and an antiferromagnetic iron chalcogenide FeTe. Our electrical transport measurements reveal interface-induced superconductivity in these heterostructures. By performing scanning tunneling microscopy and spectroscopy measurements, we observe a proximity-induced superconducting gap on the top surface of the $MnBi_2Te_4$ layer, confirming the coexistence of superconductivity and antiferromagnetism in the $MnBi_2Te_4$ layer. Our findings will advance the fundamental inquiries into the topological superconducting phase in hybrid devices and provide a promising platform for the exploration of chiral Majorana physics in $MnBi_2Te_4$-based heterostructures.

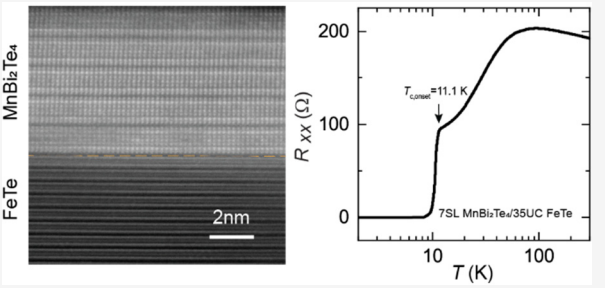

KEYWORDS: *interface-induced superconductivity, antiferromagnetism, molecular beam epitaxy growth, intrinsic magnetic topological insulator, scanning tunneling microscopy/spectroscopy*

The vitality and utility of condensed matter physics are the results of and driven by at first glance unexpected, emergent phenomena when constituent atoms, molecules, and material systems are brought together under suitable conditions. When two materials are stacked together, the resultant interface between them sometimes shows macroscopic quantum phenomena. This process of bringing out new phenomena and new electronic states of matter at the interface of two different materials is known as interface engineering. For example, the interfaces between two II−VI or III−V compound semiconductors host a two-dimensional (2D) electron gas that exhibits the celebrated integer and fractional quantum Hall effect;[1,2] when two insulating complex oxides, $LaAlO_3$ and $SrTiO_3$, are put together, superconductivity is found at their interface.[3−5] Until now, interfacial superconductors that have been searched for and identified originate predominantly from two nonmagnetic materials,[6−8] intending to avoid the potentially deleterious pair-breaking effect caused by spin-flip scattering at the interface.[9] Remarkably, interface-induced superconductivity has recently been observed in heterostructures consisting of a ferromagnetic topological insulator (TI) Cr-doped $(Bi,Sb)_2Te_3$ and an antiferromagnetic iron chalcogenide FeTe (ref.[10]). This surprising discovery motivates us to investigate whether interface-induced superconductivity can also be achieved by substituting the ferromagnetic TI with an antiferromagnetic TI.

$MnBi_2Te_4$, a tetradymite-type compound, has been demonstrated to be an intrinsic antiferromagnetic TI (refs.[11−15]) (Figures 1a and 1b). The layered antiferromagnetic order in $MnBi_2Te_4$ has a substantial influence on its topological properties. Because of the ferromagnetism within one septuple layer (SL), each helical surface state is expected to experience a magnetic exchange gap due to surface magnetization and thus contribute $e^2/2h$ to the total conductance. Depending on whether the $MnBi_2Te_4$ film has an even or odd number of SLs, the top and bottom surface magnetizations will be antiparallel or parallel and the Hall conductance from the two surfaces will cancel or sum. The total conductance is e^2/h in odd SLs [i.e., the quantum anomalous Hall (QAH) state] and 0 in even SLs (i.e., the axion insulator state) under zero magnetic field.[11,12,15−22] Both the QAH and axion insulator states have

Received: March 24, 2024
Revised: June 5, 2024
Accepted: June 12, 2024
Published: June 17, 2024

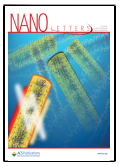

https://doi.org/10.1021/acs.nanolett.4c01407
Nano Lett. 2024, 24, 7962−7971

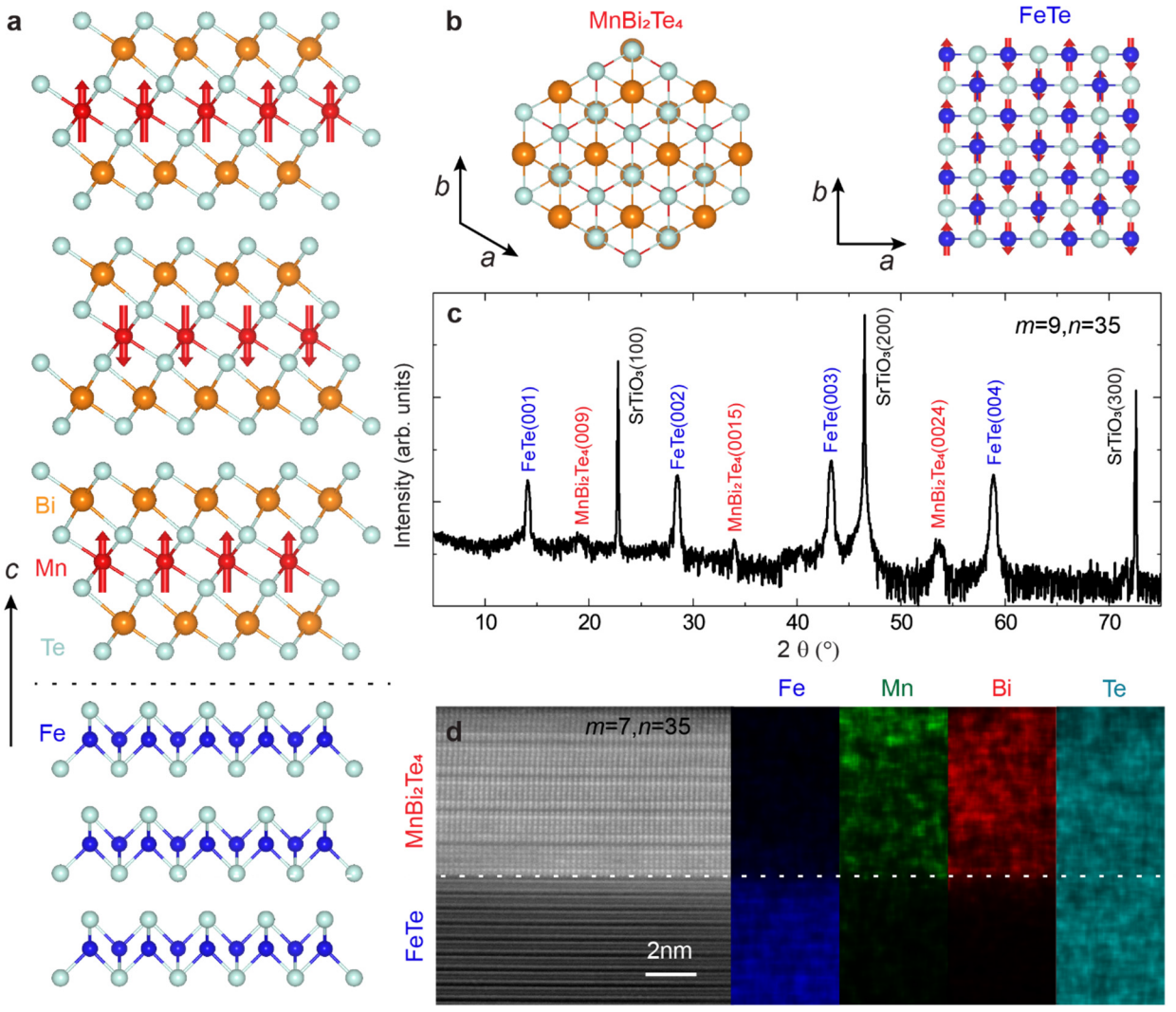

Figure 1. | MBE-grown $MnBi_2Te_4$/FeTe heterostructures. a, Side view of the $MnBi_2Te_4$/FeTe lattice structure. b, Top views of the $MnBi_2Te_4$ (left) and FeTe (right) lattice structures. The red arrows in (a) and (b) show the AFM orders in $MnBi_2Te_4$ and FeTe. c, XRD spectra of the (9, 35) heterostructure on heat-treated $SrTiO_3$(100). d, Cross-sectional STEM image and corresponding EDS maps of the (7, 35) heterostructure. A sharp interface is resolved between $MnBi_2Te_4$ and FeTe layers.

recently been observed in manually exfoliated odd- and even-SL $MnBi_2Te_4$ devices,[15,21,22] respectively. The thin films of $MnBi_2Te_4$ were also achieved by molecular beam epitaxy (MBE) growth.[13,23−29] FeTe, an antiferromagnetic iron chalcogenide that has been intensively studied in both bulk and film forms, is not superconducting without elemental doping[30,31] or tensile stress.[32] Since $MnBi_2Te_4$ and Cr-doped $(Bi,Sb)_2Te_3$ share a similar layered rhombohedral structure, a similar in-plane lattice constant, and similar growth conditions,[15] these similarities and the success in growing Cr-doped $(Bi,Sb)_2Te_3$/FeTe heterostructures[10] prompt us to grow $MnBi_2Te_4$/FeTe heterostructures to search for superconductivity at the antiferromagnet/antiferromagnet interface (Figures 1a and 1b).

In this work, we grow the heterostructures by stacking, in MBE growth, m SL $MnBi_2Te_4$ films and n unit-cell (UC) FeTe films. Below we denote m SL $MnBi_2Te_4$/n UC FeTe as the (m, n) heterostructure. The $MnBi_2Te_4$/FeTe interface is found to be atomically sharp. By performing electrical transport and scanning tunneling microscopy/spectroscopy (STM/S) measurements, we observe interface-induced superconductivity in $MnBi_2Te_4$/FeTe heterostructures and demonstrate the coexistence of superconductivity and antiferromagnetism in the $MnBi_2Te_4$ layer. Moreover, we find that the upper critical magnetic field of the emergent superconductivity is extremely high (>39.5 T) and nearly isotropic at T = 1.5 K, which may enable the coexistence of superconductivity and antiferromagnetism in our $MnBi_2Te_4$/FeTe heterostructures.

All $MnBi_2Te_4$/FeTe heterostructures are grown on heat-treated ∼0.5 mm thick $SrTiO_3$(100) substrates in a commercial MBE chamber (Omicron Lab10) . The MBE growth is monitored using *in situ* reflection high-energy electron diffraction (RHEED) (Supplementary Figure 1). The STM/S measurements are performed in a Unisoku 1300 system (310 mK, 11 T) with a base vacuum better than 3×10^{-10} mbar. The electrical transport studies are conducted in two Physical Property Measurement Systems (Quantum Design DynaCool, 1.7 K, 9 T/14 T) and a capacitor-driven 65 T pulsed magnet at the National High Magnetic Field Laboratory (NHMFL), Los Alamos. The mechanically scratched Hall bars are used for electrical transport measurements. More details about the MBE growth, sample character-

https://doi.org/10.1021/acs.nanolett.4c01407
Nano Lett. 2024, 24, 7962−7971

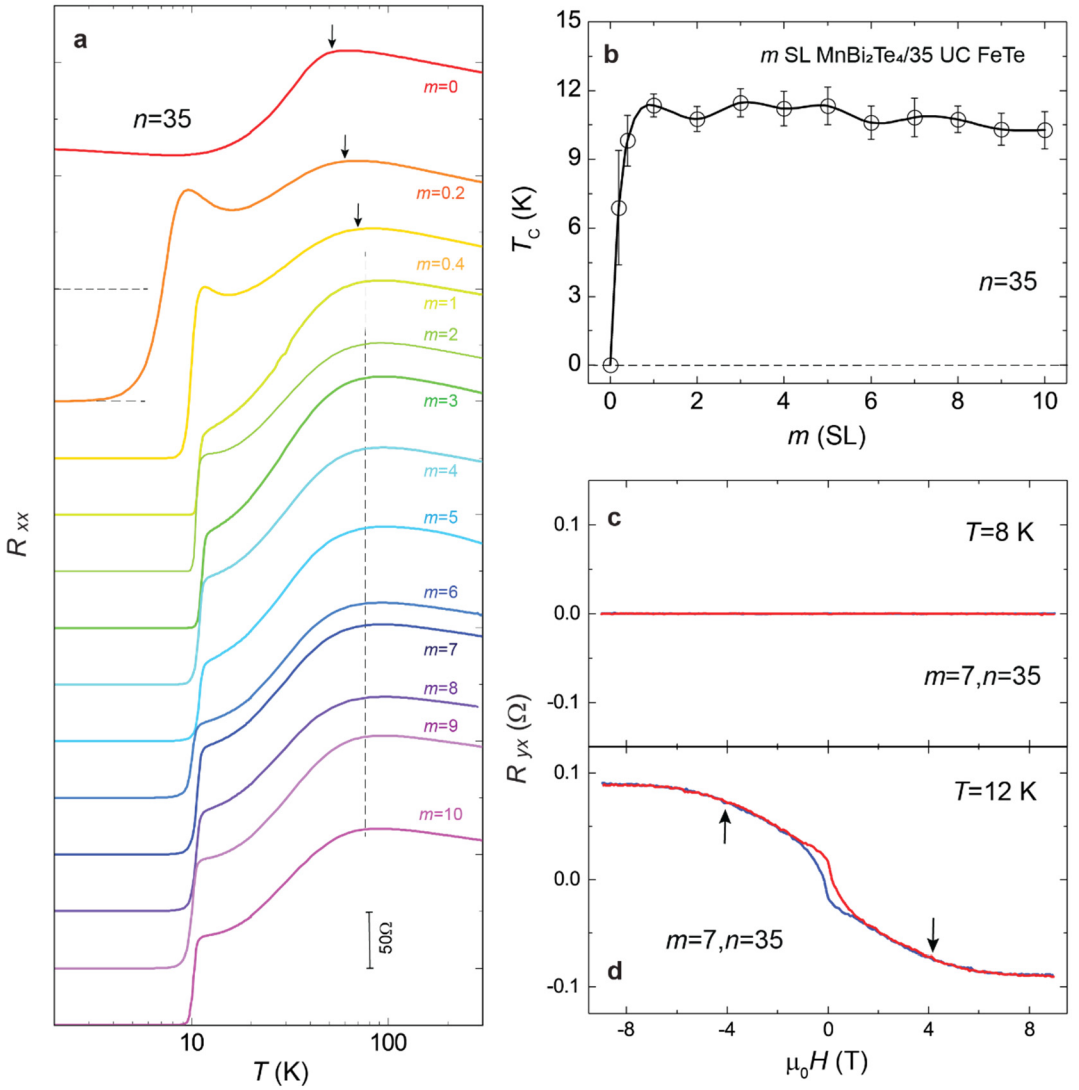

Figure 2. | Interface-induced superconductivity in $MnBi_2Te_4$/FeTe heterostructures. a, Temperature dependence of the sheet longitudinal resistance R_{xx} of the (m, 35) heterostructures with $0 \leq m \leq 10$. The two horizontal dashed lines represent zero resistance in the $m = 0$ and $m = 0.2$ heterostructures. The three arrows and the vertical dashed lines indicate the hump features resulting from the paramagnetic-to-antiferromagnetic phase transition. b, m dependence of the superconducting temperature T_c. The value of T_c is defined as the temperature at which R_{xx} drops to 50% of its normal state resistance. The error bar of each sample is estimated from the value difference between $T_{c,\,onset}$ and $T_{c,0}$. c, d, $\mu_0 H$ dependence of the Hall resistance R_{yx} of the (7, 35) heterostructure at $T = 8$ K (c) and $T = 12$ K (d). The arrows in (d) mark the kink features associated with the spin-flop transition.

ization, STM/S, and electrical transport measurements can be found in Supporting Information.

Both $MnBi_2Te_4$ and FeTe crystals are antiferromagnetic and inherently nonsuperconducting at low temperatures. $MnBi_2Te_4$ has a lattice structure composed of Te−Bi−Te−Mn−Te-Bi-Te SLs. The lattice structure of $MnBi_2Te_4$ can be viewed as intercalating a MnTe bilayer into a Bi_2Te_3 quintuple layer. Below its *Néel* temperature $T_N \sim 24$ K, $MnBi_2Te_4$ displays a layered (i.e., A-type) antiferromagnetic order due to two Mn sublattices.[13−15,33,34] As noted above, the magnetic moments of Mn atoms couple ferromagnetically within each SL, but antiferromagnetically between adjacent SLs. The magnetic moment is aligned along the c-axis (Figure 1a). For FeTe, each UC comprises one layer of Fe atoms sandwiched by two layers of Te atoms. The spins of the Fe atoms align diagonally across the Fe−Fe square lattice, giving rise to a bicollinear antiferromagnetic order (Figure 1b).[35] The formation of its antiferromagnetic order is accompanied by a structural phase transition, with the structure changing from a tetragonal to a monoclinic phase. Its *Néel* temperature T_N is in a range of 60−70 K (refs.[36−39]). Both $MnBi_2Te_4$ and FeTe are layered materials but have different lattice structures (i.e., rhombohedral vs tetragonal) (Figures 1a and 1b). We still obtain high-quality $MnBi_2Te_4$/FeTe heterostructures in our experiments.

We first characterize the $MnBi_2Te_4$/FeTe heterostructures. Supplementary Figure 1a displays the RHEED patterns of heat-treated $SrTiO_3$(100) substrate. The reconstructed RHEED patterns of the $SrTiO_3$(100) substrate show an atomically flat surface and hence suitable for MBE growth of the FeTe films. The sharp and streaky "1 × 1" RHEED patterns for $MnBi_2Te_4$ and FeTe films demonstrate the highly ordered crystal structures and the sharp interface between these two layers (Supplementary Figures 1b and 1c). Figure 1c shows the X-ray diffraction (XRD) spectra of the (9, 35)

https://doi.org/10.1021/acs.nanolett.4c01407
Nano Lett. 2024, 24, 7962−7971

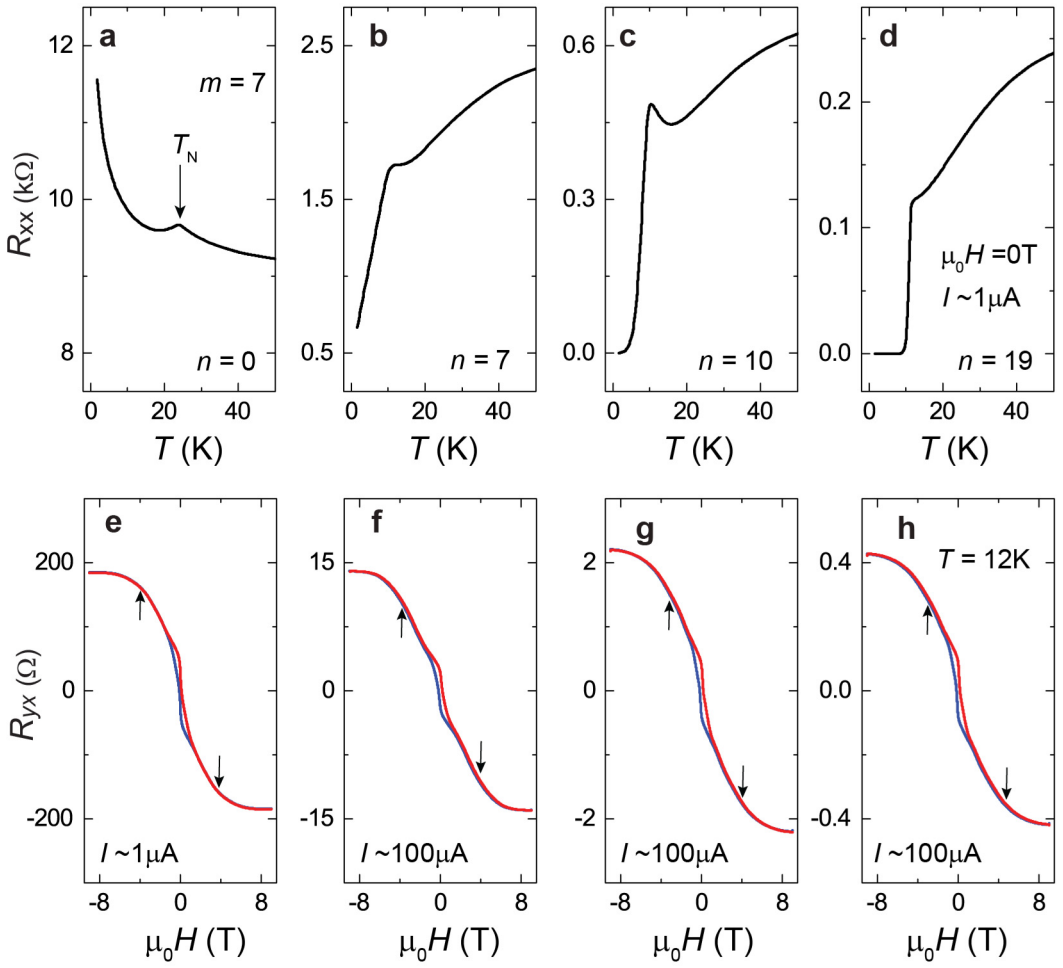

Figure 3. Transport results of the (7, *n*) heterostructures. a-d, $R_{xx} \sim T$ curves of the (7, *n*) heterostructures with $n = 0$ (a), $n = 7$ (b), $n = 10$ (c), and $n = 19$ (d). The excitation current is ~1 μA in all $R_{xx} \sim T$ measurements. For the $n = 0$ sample, a kink feature is observed at $T \sim 24$ K, which is associated with the *Néel* temperature T_N. For the $n \geq 7$ samples, interface-induced superconductivity appears. e-h, $R_{yx} \sim \mu_0 H$ curves of the (7, *n*) heterostructures with $n = 0$ (e), $n = 7$ (f), $n = 10$ (g), and $n = 19$ (h). All these measurements are performed at $T = 12$ K. The excitation current is ~1 μA for the $n = 0$ sample and ~100 μA for the $n \geq 7$ samples in all $R_{yx} \sim \mu_0 H$ measurements. The red (blue) curves represent the processes for increasing (decreasing) $\mu_0 H$. The arrows in (e-h) mark the kink features associated with the spin-flop transition.

heterostructure. Clear peaks corresponding to the $MnBi_2Te_4$ and FeTe layers, as well as $SrTiO_3(100)$ substrate are observed, confirming the high crystalline quality of our $MnBi_2Te_4$/FeTe heterostructures. Our cross-sectional scanning transmission electron microscopy (STEM) measurements resolve the highly ordered SL structure of $MnBi_2Te_4$ and the trilayer structure of FeTe, showing an atomically sharp interface (Figure 1d, Supplementary Figure 2). The atomic structures of $MnBi_2Te_4$ and FeTe layers are not simultaneously resolved, which indicates a misorientation due to their different lattice structures and symmetries. The STEM images reveal an in-plane rotation angle of ~15° between $MnBi_2Te_4$ and FeTe (Figure 1d, Supplementary Figures 2 and 3). We also perform angle-resolved photoemission spectroscopy (ARPES) measurements on the (15, 35) heterostructure (Supplementary Figure 4), which reveal a band structure similar to that of MBE-grown $MnBi_2Te_4$ films on $SrTiO_3(111)$ (ref.[25]).

To investigate the interface-induced superconductivity in heterostructures formed by stacking together antiferromagnetic $MnBi_2Te_4$ and FeTe layers, we maintain the thickness of the FeTe layer at $n = 35$ and grow a series of the (m, 35) heterostructures with $0 \leq m \leq 10$. The specific value of m is determined by the growth duration and then calibrated by the atomic force microscopy measurements. Note that the top $MnBi_2Te_4$ layer with $m < 1$ indicates the partial coverage of 1 SL $MnBi_2Te_4$ islands on the FeTe layer.[15,25] We perform electrical transport measurements on these (m, 35) heterostructures. For the $m = 0$ sample, i.e., the 35 UC FeTe layer, the R_{xx}-T curve shows a nonsuperconducting behavior (Figure 2a). This observation is also confirmed by the absence of the superconducting gap in the dI/dV spectra measured on the top surface of the FeTe layer (Figure 4c). A hump feature, which is usually associated with the paramagnetic-to-antiferromagnetic phase transition (i.e., T_N), is observed at $T \sim 62$ K (Figure 2a). Once the $MnBi_2Te_4$ layer with a thickness of 0.2 SL is deposited onto the 35 UC FeTe layer, superconductivity emerges. For the $m = 0.2$ sample, the zero-resistance state appears below $T_{c,0} \sim 3.6$ K, while the superconducting onset temperature $T_{c,onset}$ is ~8.6 K. Here $T_{c,onset}$ is defined when R_{xx} begins its drop from the normal state value. With a further increase in m, $T_{c,onset}$ exhibits a slight increase, while $T_{c,0}$ shows a much more significant enhancement. Specifically, for the $m = 0.4$ sample, $T_{c,0} \sim 8.6$ K and $T_{c,onset} \sim 10.6$ K. Both $T_{c,0}$ and $T_{c,onset}$ values reach saturation for $m \geq 1$ (Figure 2a).

Moreover, we observe that the T_N hump feature broadens with increasing m and eventually reaches saturation for $m \geq 1$,

https://doi.org/10.1021/acs.nanolett.4c01407
Nano Lett. 2024, 24, 7962−7971

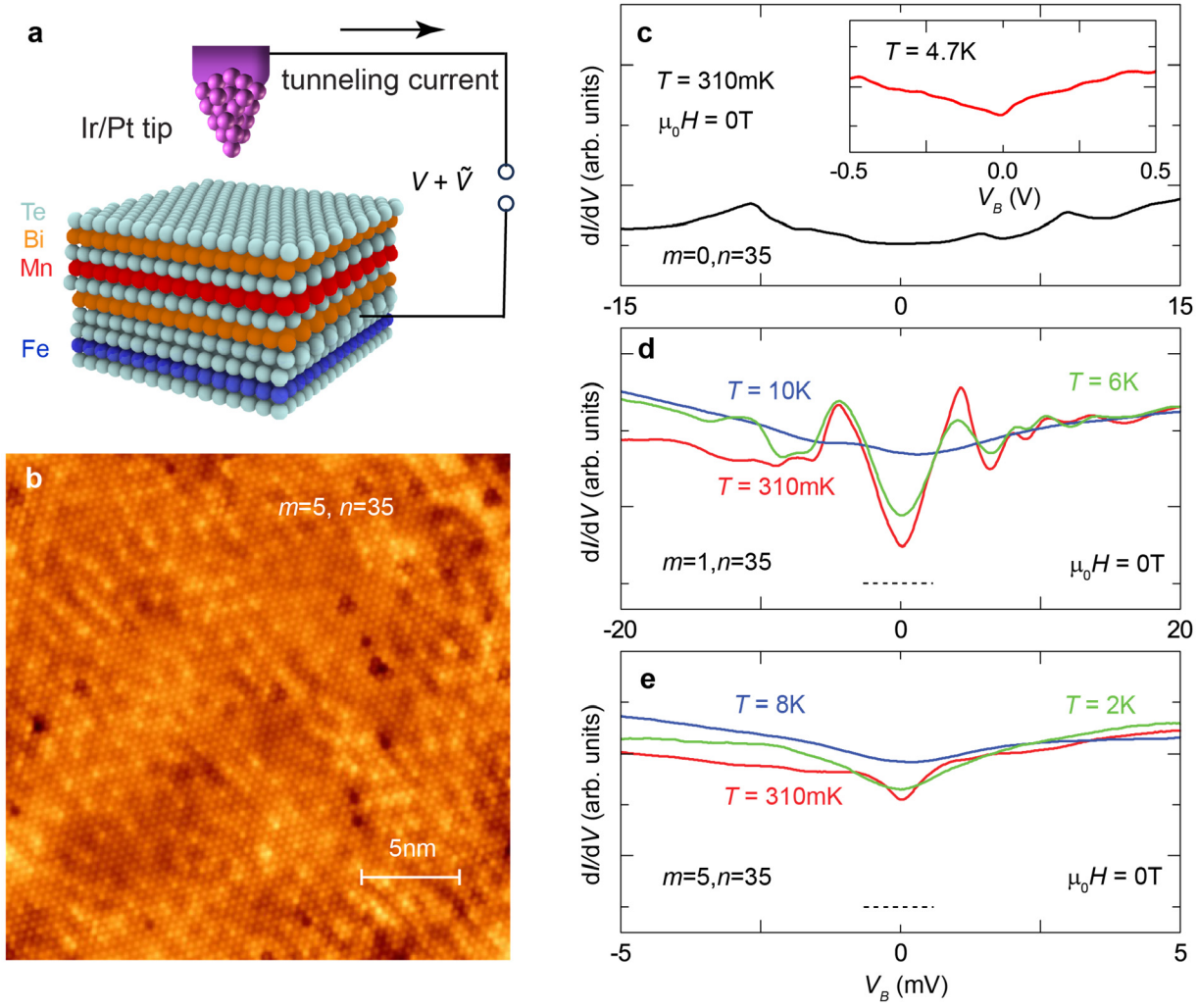

Figure 4. | STM/S characterization of*m*SL $MnBi_2Te_4$/35 UC FeTe heterostructures. a, Schematic of the STM/S measurement. b, Atomic resolution STM image of the (5, 35) heterostructure (sample bias $V_B = -300$ mV, tunneling current $I_t = 1000$ pA, $T = 310$ mK). c, dI/dV spectra on the surface of the pristine FeTe film with the range of 15 mV (set point: $V_B = +15$ mV, $I_t = 1000$ pA, $T = 310$ mK). Inset: dI/dV spectra with the range of 0.5 V (set point: $V_B = +500$ mV, $I_t = 500$ pA, $T = 4.7$ K). d, dI/dV spectra on the top surface of the (1, 35) heterostructure at different temperatures (set point: $V_B = +20$ mV, $I_t = 300$ pA). e, dI/dV spectra on the top surface of the (5, 35) heterostructure measured at different temperatures (set point: $V_B = +5$ mV, $I_t = 300$pA). The dashed lines in (d) and (e) correspond to the zero dI/dV values of (1, 35) and (5, 35) heterostructures, respectively.

indicating the suppression of antiferromagnetism. This suggests that the suppression of antiferromagnetism in the FeTe layer is linked to the emergence of interface-induced superconductivity. In our $MnBi_2Te_4$/FeTe heterostructures, the bottom FeTe layer is an antiferromagnetic metal, and superconductivity can emerge after its antiferromagnetic order is weakened by either elemental doping[30,31] or tensile stress.[32] The charge carrier transfer and/or strain effect across the $MnBi_2Te_4$/FeTe interface might suppress the antiferromagnetic order, triggering the formation of this interface-induced superconductivity. Moreover, the Ruderman−Kittel−Kasuya−Yosida (RKKY) interactions from the spin-momentum locked topological surface states, coupled with the interfacial FeTe layer, may also destabilize the antiferromagnetic order in the FeTe layer and thus promote superconductivity.[40] Note that the suppression of the antiferromagnetism in our $MnBi_2Te_4$/FeTe heterostructures is primarily indicated by the broadening of the T_N hump feature. For the $m = 7$ sample, both $T_{c,onset}$ and $T_{c,0}$ reach maximum values of ∼11.1 K and ∼9.2 K, respectively (Figure 2a). For a straightforward comparison of different samples, we define the superconducting transition temperature T_c as the temperature at which R_{xx} drops to ∼50% of its normal state value of $T = 20$ K and plot the T_c values as a function of m (Figure 2b). For $m \leq 1$, we observe a significant increase in T_c with increasing m. However, for $m \geq 1$, the T_c values show a weak fluctuation, consistent with the above analysis.

To demonstrate the presence of antiferromagnetism in the $MnBi_2Te_4$ layer, we carry out Hall measurements on the (7, 35) heterostructure at different temperatures (Figures 2c and 2d, Supplementary Figure 5). At $T = 8$ K, which is below its $T_{c,0} \sim 9.2$ K, the Hall resistance R_{yx} is vanishing, which is a result of the zero-resistance state of the superconducting phase (Figure 2c). At $T = 12$ K, which is slightly greater than $T_{c,onset} \sim 11.1$ K, a nonsquare hysteresis loop is observed (Figure 2d). This nonsquare hysteresis loop of the $MnBi_2Te_4$ films can be separated into two anomalous Hall components. One with a larger coercive field is from the dominant $MnBi_2Te_4$ phase, while the other with the smaller coercive field is from the minor Mn-doped Bi_2Te_3 phase.[25] Therefore, the small

https://doi.org/10.1021/acs.nanolett.4c01407
Nano Lett. 2024, 24, 7962−7971

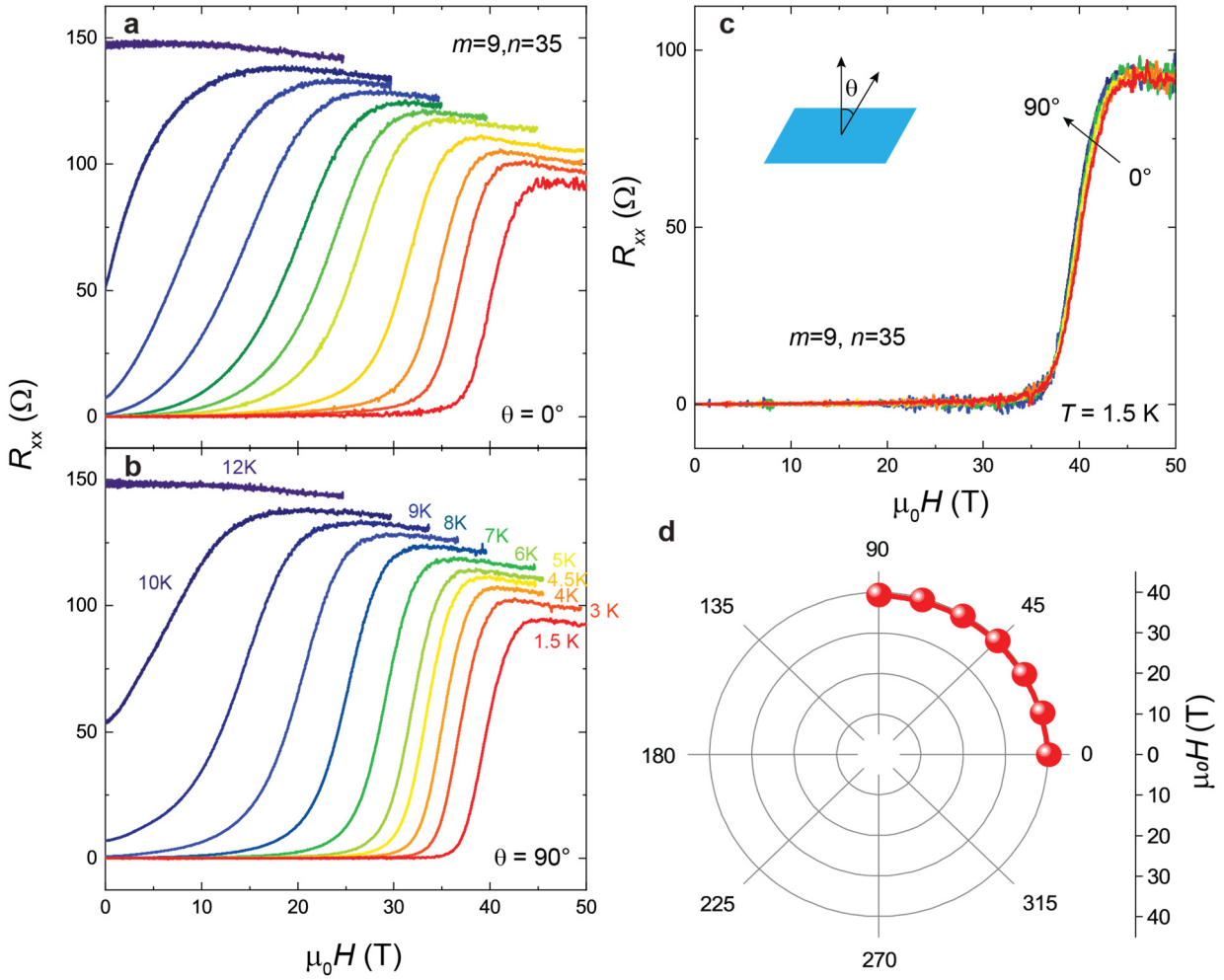

Figure 5. | Large and isotropic upper critical magnetic field in $MnBi_2Te_4$/FeTe heterostructures. a, b, R_{xx}-$\mu_0 H$ curves of the (9, 35) heterostructure under different T (a) $\theta = 0°$ (i.e., out-of-plane) and (b) $\theta = 90°$ (i.e., in-plane). c, R_{xx}-$\mu_0 H$ curves of the same (9, 35) heterostructure at $T = 1.5$ K under different θ. Inset shows the angle θ between the normal direction of the film and the magnetic field $\mu_0 H$ direction. d, θ dependence of the upper critical magnetic field $\mu_0 H_{c2}$. The value of $\mu_0 H_{c2}$ is determined as the magnetic field at which R_{xx} drops to ~50% of its normal state value.

nonsquare hysteresis loop observed in the (7, 35) heterostructure is presumably induced by the uncompensated magnetization in the dominant $MnBi_2Te_4$ phase[41,42] and/or the minor ferromagnetic Mn-doped Bi_2Te_3 phase.[25] A kink feature, associated with the spin-flop transition, has been employed in some studies to identify the antiferromagnetism in the MBE-grown $MnBi_2Te_4$ layer.[13,15,23−29] This kink feature is not well resolved in the (7, 35) heterostructure (Figure 2d), possibly due to the following two reasons: (*i*) the measurement temperature needs to exceed its $T_{c,onset} \sim 11.1$ K; and (*ii*) the high conductivity of the bottom 35 UC FeTe layer may divert current flow within the heterostructure sample. However, at $T = 12$ K, the overall shape of the Hall traces for the (7, 35) heterostructure (Figure 2d, Supplementary Figure 5b) closely resembles that of 7 SL $MnBi_2Te_4$ without the bottom FeTe layer (Figure 3e). Furthermore, the nonsquare hysteresis loop near zero magnetic field disappears at $T = 25$ K (Supplementary Figure 5e), consistent with the T_N value of 7 SL $MnBi_2Te_4$. Both observations indicate the persistence of antiferromagnetism within the $MnBi_2Te_4$ layer in the heterostructure samples.

Besides varying m at $n = 35$, we also fix $m = 7$ and perform electrical transport measurements on the (7, n) $MnBi_2Te_4$/FeTe heterostructures with different n. For the $n = 0$ sample, i.e., 7 SL $MnBi_2Te_4$ film on $SrTiO_3$(111) substrate grown by the same recipe, a hump feature is observed at $T \sim 24$ K, which suggests $T_N \sim 24$ K of the 7SL $MnBi_2Te_4$ film (Figure 3a). For $T \leq 15$ K, R_{xx} exhibits an abrupt increase, which is probably attributable to the insulating ground state induced by electron−electron interaction in TI thin films.[43,44] With a further increase in n, R_{xx} gradually decreases, and the interface-induced superconductivity progressively becomes unmistakable (Figures 3b to 3d). As we noted above, the absence of the T_N hump feature for $n \geq 7$ is probably due to the much higher conductivity of the bottom FeTe layer compared to the top 7 SL $MnBi_2Te_4$ layer.

The (7, 7) heterostructure shows an onset of superconductivity near ~10.5 K without ever reaching a zero-resistance state. This indicates a lack of true long-range superconducting coherence within this thinner FeTe film (Figure 3b). At $T = 12$ K, the Hall traces of the (7, 7) heterostructure resemble those of the (7, 0) heterostructure but shrink by 1 order of magnitude (Figures 3e and 3f). The spin-flop transition kink feature is also observed near $\mu_0 H \sim \pm 4.0$ T (Figure 3f). With a further increase in n, the conductivity of the FeTe layer is enhanced, and thus more electrical current flows through the bottom FeTe layer. Therefore, the Hall traces of the (7, n) heterostructures further shrink but the spin-

https://doi.org/10.1021/acs.nanolett.4c01407
Nano Lett. 2024, 24, 7962−7971

flop transition kink feature is still observed at T = 12 K (Figures 3e to 3h). These observations further confirm the antiferromagnetic property of the top 7 SL $MnBi_2Te_4$ layer.

To validate the proximity-induced superconducting gap on the top surface of the $MnBi_2Te_4$ layer, we perform low-temperature STM/S measurements on three (m, 35) heterostructures with m = 0, 1, and 5 (Figure 4a). Figure 4b shows the STM topographic image with atomic resolution of the (5, 35) heterostructure. We can clearly see hexagonal close-packed Te atoms on the top surface of the 5 SL $MnBi_2Te_4$ layer. The triangle-shaped dark features are the Mn/Bi antisites in the $MnBi_2Te_4$ layer.[45] On the top surface of the m = 0 heterostructure, i.e., the 35 UC FeTe layer, no superconducting gap is observed near zero sample bias (Figure 4c), consistent with its R_{xx}-T curve (Figure 2a).

Upon deposition of 1 SL $MnBi_2Te_4$ on the 35 UC FeTe layer, superconductivity appears. For the (1, 35) heterostructure, we observe a proximity-induced superconducting gap on the top surface of the 1 SL $MnBi_2Te_4$ layer (Figure 4d, Supplementary Figures 6 and 7). This observation is in good agreement with our transport results (Figure 2). At T = 310 mK, the superconducting gap size is ∼2.9 meV, which is determined from the fit using the Dynes formula (Supplementary Figure 6).[46] With increasing T, the proximity-induced superconducting gap gradually diminishes and ultimately vanishes at T = 12.3 K (Figure 4d, Supplementary Figures 7a and 7c). With a further increase in m, the proximity-induced superconductivity is attenuated on the top surface of the $MnBi_2Te_4$ layer. For the (5, 35) heterostructure, we observe a narrower and shallower superconducting gap at T = 310 mK (Figure 4e). This observation further confirms that the superconducting gap observed on the top surface of the $MnBi_2Te_4$ layer is indeed induced by the proximity effect. With increasing T, this superconducting gap shrinks faster and disappears at T = 3.0 K (Figure 4e, Supplementary Figures 7b and 7c). Furthermore, our low energy muon spin relaxation (LE-μSR) measurements on the (7, 35) heterostructure also support a uniform antiferromagnetic order in the $MnBi_2Te_4$ layer, which is achieved above $T_{c,onset}$ and persists below $T_{c,0}$ (Supplementary Figure 10). By combining electrical transport with STM/S and LE-μSR results, we demonstrate the coexistence of intrinsic antiferromagnetism and proximity-induced superconductivity in the $MnBi_2Te_4$ layer.

Next, we perform electrical transport measurements on the (9, 35) heterostructure under high magnetic fields to further our understanding of the coexistence of superconductivity and antiferromagnetism in $MnBi_2Te_4$/FeTe heterostructures. Figures 5a and 5b show the R_{xx}-μ_0H curves at different temperatures with θ = 0° and 90°, respectively. Here θ is defined as the angle between the normal direction of the sample plane and the direction of μ_0H (Figure 5c inset). We observe similar behaviors in these R_{xx}-μ_0H curves at θ = 0° and 90° under different temperatures. At T = 1.5 K, R_{xx} remains zero until μ_0H reaches ∼32.8 T. Subsequently, R_{xx} dramatically increases and transitions to the normal state near μ_0H ∼ 45.0 T (Figures 5a and 5b). To examine the anisotropy of interface-induced superconductivity in $MnBi_2Te_4$/FeTe heterostructures, we measure the R_{xx}-μ_0H curves of the (9, 35) heterostructure at different θ and T = 1.5 K. We find that the R_{xx}-μ_0H curves show nearly identical behavior under all θ implying the interface-induced superconductivity in $MnBi_2Te_4$/FeTe heterostructures is isotropic (Figure 5c). We define the upper critical magnetic field μ_0H_{c2} as the magnetic field at which R_{xx} drops to ∼50% of its normal state value. The value of μ_0H_{c2} is ∼39.5 T under different θ (Figure 5d). The isotropic angle dependence suggests the interface-induced superconductivity is bulk-like in our $MnBi_2Te_4$/FeTe heterostructures. We note that these features are consistent with our recent findings in Cr-doped $(Bi, Sb)_2Te_3$/FeTe heterostructures,[10] verifying that the emergent superconductivity originates from the FeTe layer. Moreover, we note that the large μ_0H_{c2} may be the key condition that allows for the coexistence of superconductivity and antiferromagnetism in the $MnBi_2Te_4$ layer. Further experimental and theoretical studies are needed to clarify this point.

To summarize, we employ MBE to synthesize $MnBi_2Te_4$/FeTe heterostructures and discover an emergent interface-induced superconductivity formed by stacking together two antiferromagnetic layers. By performing electrical transport and STM/S measurements, we demonstrate the coexistence of superconductivity and antiferromagnetism within the $MnBi_2Te_4$ layer. Furthermore, we find that the upper critical magnetic field of the interface-induced superconductivity in $MnBi_2Te_4$/FeTe heterostructures is large and isotropic, which may be responsible for the coexistence of superconductivity and antiferromagnetism. The MBE-grown $MnBi_2Te_4$/FeTe heterostructures with robust interface-induced superconductivity and atomically sharp interfaces provide a promising platform for the exploration of chiral Majorana physics[47−49] and thus constitute an important step toward scalable topological quantum computation.

■ ASSOCIATED CONTENT

Supporting Information

The Supporting Information is available free of charge at https://pubs.acs.org/doi/10.1021/acs.nanolett.4c01407.

MBE growth of the $MnBi_2Te_4$/FeTe heterostructures, XRD, STEM, and ARPES measurements, Hall bar device fabrication, electrical transport measurements, STM/S measurements, and LE-μSR measurement (PDF)

■ AUTHOR INFORMATION

Corresponding Author

Cui-Zu Chang − *Department of Physics, The Pennsylvania State University, University Park, Pennsylvania 16802, United States;* orcid.org/0000-0003-3515-2955; Email: cxc955@psu.edu

Authors

Wei Yuan − *Department of Physics, The Pennsylvania State University, University Park, Pennsylvania 16802, United States*

Zi-Jie Yan − *Department of Physics, The Pennsylvania State University, University Park, Pennsylvania 16802, United States;* orcid.org/0000-0001-6176-319X

Hemian Yi − *Department of Physics, The Pennsylvania State University, University Park, Pennsylvania 16802, United States*

Zihao Wang − *Department of Physics, The Pennsylvania State University, University Park, Pennsylvania 16802, United States;* orcid.org/0009-0005-9734-8816

Stephen Paolini − *Department of Physics, The Pennsylvania State University, University Park, Pennsylvania 16802, United States*

https://doi.org/10.1021/acs.nanolett.4c01407
Nano Lett. 2024, 24, 7962−7971

Yi-Fan Zhao − *Department of Physics, The Pennsylvania State University, University Park, Pennsylvania 16802, United States*
Lingjie Zhou − *Department of Physics, The Pennsylvania State University, University Park, Pennsylvania 16802, United States*
Annie G. Wang − *Department of Physics, The Pennsylvania State University, University Park, Pennsylvania 16802, United States*
Ke Wang − *Materials Research Institute, The Pennsylvania State University, University Park, Pennsylvania 16802, United States*
Thomas Prokscha − *Laboratory for Muon Spectroscopy, Paul Scherrer Institute, 5232 Villigen PSI, Switzerland*
Zaher Salman − *Laboratory for Muon Spectroscopy, Paul Scherrer Institute, 5232 Villigen PSI, Switzerland*
Andreas Suter − *Laboratory for Muon Spectroscopy, Paul Scherrer Institute, 5232 Villigen PSI, Switzerland*
Purnima P. Balakrishnan − *NIST Center for Neutron Research, National Institute of Standards and Technology, Gaithersburg, Maryland 20899, United States;* orcid.org/0000-0002-1426-669X
Alexander J. Grutter − *NIST Center for Neutron Research, National Institute of Standards and Technology, Gaithersburg, Maryland 20899, United States;* orcid.org/0000-0002-6876-7625
Laurel E. Winter − *National High Magnetic Field Laboratory, Los Alamos, New Mexico 87544, United States*
John Singleton − *National High Magnetic Field Laboratory, Los Alamos, New Mexico 87544, United States;* orcid.org/0000-0001-6109-6905
Moses H. W. Chan − *Department of Physics, The Pennsylvania State University, University Park, Pennsylvania 16802, United States*

Complete contact information is available at: https://pubs.acs.org/10.1021/acs.nanolett.4c01407

Author Contributions

[¶]W.Y. and Z.-J.Y. contributed equally. C.-Z.C. conceived and designed the experiment. W.Y., Z.-J.Y., H.Y., L.-J.Z., and A.G.W. performed the MBE growth and PPMS transport measurements. Z.-J.Y. performed the XRD measurements. K.W. and H.Y. carried out the STEM measurements. H.Y. and Z.-J.Y. performed the ARPES measurements. Z.W., S.P., and Y.-F.Z. performed STM/S measurements. H.Y., J.S., and L.E.W. performed the electrical transport measurements at NHMFL, Los Alamos. T.P., Z.S., A.S., P.P.B., and A.J.G. performed the μSR measurements. W.Y., Z.-J.Y., and C.-Z.C. analyzed the data and wrote the manuscript with input from all authors.

Notes

The authors declare no competing financial interest.

ACKNOWLEDGMENTS

This work is primarily supported by the DOE grant (DE-SC0023113), including the MBE growth and PPMS (9T) measurements. The XRD, STEM, and PPMS (14T) measurements are partially supported by the NSF-CAREER award (DMR-1847811) and the Penn State MRSEC for Nanoscale Science (DMR-2011839). The STM/S measurements are partially supported by the ARO grant (W911NF2210159). C.-Z. C. acknowledges the support from the Gordon and Betty Moore Foundation's EPiQS Initiative (Grant GBMF9063 to C. -Z. C.). Work done at NHMFL is supported by NSF (DMR-2128556) (J. S. and L. E. W.) and the State of Florida.

REFERENCES

(1) Klitzing, K. v.; Dorda, G.; Pepper, M. New Method for High-Accuracy Determination of the Fine-Structure Constant Based on Quantized Hall Resistance. *Phys. Rev. Lett.* **1980**, *45*, 494−497.
(2) Tsui, D. C.; Stormer, H. L.; Gossard, A. C. Two-Dimensional Magnetotransport in the Extreme Quantum Limit. *Phys. Rev. Lett.* **1982**, *48*, 1559−1562.
(3) Ohtomo, A.; Hwang, H. Y. A high-mobility electron gas at the $LaAlO_3/SrTiO_3$ heterointerface. *Nature* **2004**, *427*, 423−426.
(4) Reyren, N.; Thiel, S.; Caviglia, A. D.; Kourkoutis, L. F.; Hammerl, G.; Richter, C.; Schneider, C. W.; Kopp, T.; Ruetschi, A. S.; Jaccard, D.; Gabay, M.; Muller, D. A.; Triscone, J. M.; Mannhart, J. Superconducting interfaces between insulating oxides. *Science* **2007**, *317*, 1196−1199.
(5) Gozar, A.; Logvenov, G.; Kourkoutis, L. F.; Bollinger, A. T.; Giannuzzi, L. A.; Muller, D. A.; Bozovic, I. High-temperature interface superconductivity between metallic and insulating copper oxides. *Nature* **2008**, *455*, 782−785.
(6) Wang, L. L.; Ma, X. C.; Xue, Q. K. Interface high-temperature superconductivity. *Supercon. Sci. Technol.* **2016**, *29*, 123001.
(7) Gozar, A.; Bozovic, I. High temperature interface superconductivity. *Physica C* **2016**, *521*, 38−49.
(8) Gariglio, S.; Gabay, M.; Mannhart, J.; Triscone, J. M. Interface superconductivity. *Physica C* **2015**, *514*, 189−198.
(9) Buzdin, A. I. Proximity effects in superconductor-ferromagnet heterostructures. *Rev. Mod. Phys.* **2005**, *77*, 935−976.
(10) Yi, H.; Zhao, Y.-F.; Chan, Y.-T.; Cai, J.; Mei, R.; Wu, X.; Yan, Z.-J.; Zhou, L.-J.; Zhang, R.; Wang, Z.; Paolini, S.; Xiao, R.; Wang, K.; Richardella, A. R.; Singleton, J.; Winter, L. E.; Prokscha, T.; Salman, Z.; Suter, A.; Balakrishnan, P. P.; Grutter, A. J.; Chan, M. H. W.; Samarth, N.; Xu, X.; Wu, W.; Liu, C.-X.; Chang, C.-Z. Interface-Induced Superconductivity in Magnetic Topological Insulators. *Science* **2024**, *383*, 634−639.
(11) Li, J. H.; Li, Y.; Du, S. Q.; Wang, Z.; Gu, B. L.; Zhang, S. C.; He, K.; Duan, W. H.; Xu, Y. Intrinsic Magnetic Topological Insulators in van der Waals Layered $MnBi_2Te_4$-Family Materials. *Sci. Adv.* **2019**, *5*, No. eaaw5685.
(12) Zhang, D. Q.; Shi, M. J.; Zhu, T. S.; Xing, D. Y.; Zhang, H. J.; Wang, J. Topological Axion States in the Magnetic Insulator $MnBi_2Te_4$ with the Quantized Magnetoelectric Effect. *Phys. Rev. Lett.* **2019**, *122*, 206401.
(13) Gong, Y.; Guo, J. W.; Li, J. H.; Zhu, K. J.; Liao, M. H.; Liu, X. Z.; Zhang, Q. H.; Gu, L.; Tang, L.; Feng, X.; Zhang, D.; Li, W.; Song, C. L.; Wang, L. L.; Yu, P.; Chen, X.; Wang, Y. Y.; Yao, H.; Duan, W. H.; Xu, Y.; Zhang, S. C.; Ma, X. C.; Xue, Q. K.; He, K. Experimental Realization of an Intrinsic Magnetic Topological Insulator. *Chin. Phys. Lett.* **2019**, *36*, 076801.
(14) Otrokov, M. M.; Klimovskikh, I. I.; Bentmann, H.; Estyunin, D.; Zeugner, A.; Aliev, Z. S.; Gass, S.; Wolter, A. U. B.; Koroleva, A. V.; Shikin, A. M.; Blanco-Rey, M.; Hoffmann, M.; Rusinov, I. P.; Vyazovskaya, A. Y.; Eremeev, S. V.; Koroteev, Y. M.; Kuznetsov, V. M.; Freyse, F.; Sanchez-Barriga, J.; Amiraslanov, I. R.; Babanly, M. B.; Mamedov, N. T.; Abdullayev, N. A.; Zverev, V. N.; Alfonsov, A.; Kataev, V.; Buchner, B.; Schwier, E. F.; Kumar, S.; Kimura, A.; Petaccia, L.; Di Santo, G.; Vidal, R. C.; Schatz, S.; Kissner, K.; Unzelmann, M.; Min, C. H.; Moser, S.; Peixoto, T. R. F.; Reinert, F.; Ernst, A.; Echenique, P. M.; Isaeva, A.; Chulkov, E. V. Prediction and observation of an antiferromagnetic topological insulator. *Nature* **2019**, *576*, 416−422.
(15) Chang, C.-Z.; Liu, C.-X.; MacDonald, A. H. Colloquium: Quantum anomalous Hall effect. *Rev. Mod. Phys.* **2023**, *95*, 011002.
(16) Otrokov, M. M.; Rusinov, I. P.; Blanco-Rey, M.; Hoffmann, M.; Vyazovskaya, A. Y.; Eremeev, S. V.; Ernst, A.; Echenique, P. M.; Arnau, A.; Chulkov, E. V. Unique Thickness-Dependent Properties of

the van der Waals Interlayer Antiferromagnet $MnBi_2Te_4$ Films. *Phys. Rev. Lett.* **2019**, *122*, 107202.
(17) Chang, C. Z.; Zhang, J. S.; Feng, X.; Shen, J.; Zhang, Z. C.; Guo, M. H.; Li, K.; Ou, Y. B.; Wei, P.; Wang, L. L.; Ji, Z. Q.; Feng, Y.; Ji, S. H.; Chen, X.; Jia, J. F.; Dai, X.; Fang, Z.; Zhang, S. C.; He, K.; Wang, Y. Y.; Lu, L.; Ma, X. C.; Xue, Q. K. Experimental Observation of the Quantum Anomalous Hall Effect in a Magnetic Topological Insulator. *Science* **2013**, *340*, 167−170.
(18) Yu, R.; Zhang, W.; Zhang, H. J.; Zhang, S. C.; Dai, X.; Fang, Z. Quantized Anomalous Hall Effect in Magnetic Topological Insulators. *Science* **2010**, *329*, 61−64.
(19) Xiao, D.; Jiang, J.; Shin, J. H.; Wang, W. B.; Wang, F.; Zhao, Y. F.; Liu, C. X.; Wu, W. D.; Chan, M. H. W.; Samarth, N.; Chang, C. Z. Realization of the Axion Insulator State in Quantum Anomalous Hall Sandwich Heterostructures. *Phys. Rev. Lett.* **2018**, *120*, 056801.
(20) Mogi, M.; Kawamura, M.; Tsukazaki, A.; Yoshimi, R.; Takahashi, K. S.; Kawasaki, M.; Tokura, Y. Tailoring Tricolor Structure of Magnetic Topological Insulator for Robust Axion Insulator. *Sci. Adv.* **2017**, *3*, No. eaao1669.
(21) Liu, C.; Wang, Y. C.; Li, H.; Wu, Y.; Li, Y. X.; Li, J. H.; He, K.; Xu, Y.; Zhang, J. S.; Wang, Y. Y. Robust axion insulator and Chern insulator phases in a two-dimensional antiferromagnetic topological insulator. *Nat. Mater.* **2020**, *19*, 522−527.
(22) Deng, Y.; Yu, Y.; Shi, M. Z.; Guo, Z.; Xu, Z.; Wang, J.; Chen, X. H.; Zhang, Y. Quantum anomalous Hall effect in intrinsic magnetic topological insulator $MnBi_2Te_4$. *Science* **2020**, *367*, 895−900.
(23) Rienks, E. D. L.; Wimmer, S.; Sanchez-Barriga, J.; Caha, O.; Mandal, P. S.; Ruzicka, J.; Ney, A.; Steiner, H.; Volobuev, V. V.; Groiss, H.; Albu, M.; Kothleitner, G.; Michalicka, J.; Khan, S. A.; Minar, J.; Ebert, H.; Bauer, G.; Freyse, F.; Varykhalov, A.; Rader, O.; Springholz, G. Large magnetic gap at the Dirac point in Bi_2Te_3/$MnBi_2Te_4$ heterostructures. *Nature* **2019**, *576*, 423−428.
(24) Zhu, K. J.; Bai, Y. H.; Hong, X. Y.; Geng, Z. H.; Jiang, Y. Y.; Liu, R. X.; Li, Y. Z.; Shi, M.; Wang, L. L.; Li, W.; Xue, Q. K.; Feng, X.; He, K. Investigating and manipulating the molecular beam epitaxy growth kinetics of intrinsic magnetic topological insulator $MnBi_2Te_4$ with *in situ* angle-resolved photoemission spectroscopy. *J. Phys.: Condens. Matter* **2020**, *32*, 475002.
(25) Zhao, Y. F.; Zhou, L. J.; Wang, F.; Wang, G.; Song, T. C.; Ovchinnikov, D.; Yi, H. M.; Mei, R. B.; Wang, K.; Chan, M. H. W.; Liu, C. X.; Xu, X. D.; Chang, C. Z. Even-Odd Layer-Dependent Anomalous Hall Effect in Topological Magnet $MnBi_2Te_4$ Thin Films. *Nano Lett.* **2021**, *21*, 7691−7698.
(26) Bac, S. K.; Koller, K.; Lux, F.; Wang, J.; Riney, L.; Borisiak, K.; Powers, W.; Zhukovskyi, M.; Orlova, T.; Dobrowolska, M.; Furdyna, J. K.; Dilley, N. R.; Rokhinson, L. P.; Mokrousov, Y.; McQueeney, R. J.; Heinonen, O.; Liu, X.; Assaf, B. A. Topological response of the anomalous Hall effect in $MnBi_2Te_4$ due to magnetic canting. *npj Quantum Mater.* **2022**, *7*, 46.
(27) Trang, C. X.; Li, Q. L.; Yin, Y. F.; Hwang, J.; Akhgar, G.; Di Bernardo, I.; Grubisic-Cabo, A.; Tadich, A.; Fuhrer, M. S.; Mo, S. K.; Medhekar, N. V.; Edmonds, M. T. Crossover from 2D Ferromagnetic Insulator to Wide Band Gap Quantum Anomalous Hall Insulator in Ultrathin $MnBi_2Te_4$. *ACS Nano* **2021**, *15*, 13444−13452.
(28) Lapano, J.; Nuckols, L.; Mazza, A. R.; Pai, Y. Y.; Zhang, J.; Lawrie, B.; Moore, R. G.; Eres, G.; Lee, H. N.; Du, M. H.; Ward, T. Z.; Lee, J. S.; Weber, W. J.; Zhang, Y. W.; Brahlek, M. Adsorption-controlled growth of $MnTe(Bi_2Te_3)_n$ by molecular beam epitaxy exhibiting stoichiometry-controlled magnetism. *Phys. Rev. Mater.* **2020**, *4*, 111201.
(29) Bai, Y. H.; Li, Y. Z.; Luan, J. L.; Liu, R. X.; Song, W. Y.; Chen, Y.; Ji, P. F.; Zhang, Q. H.; Meng, F. Q.; Tong, B. B.; Li, L.; Jiang, Y. Y.; Gao, Z. W.; Gu, L.; Zhang, J. S.; Wang, Y. Y.; Xue, Q. K.; He, K.; Feng, Y.; Feng, X. Quantized anomalous Hall resistivity achieved in molecular beam epitaxy-grown $MnBi_2Te_4$ thin films. *Natl. Sci. Rev.* **2024**, *11*, nwad189.
(30) Mizuguchi, Y.; Tomioka, F.; Tsuda, S.; Yamaguchi, T.; Takano, Y. Superconductivity in S-substituted FeTe. *Appl. Phys. Lett.* **2009**, *94*, 012503.
(31) Li, F. S.; Ding, H.; Tang, C. J.; Peng, J. P.; Zhang, Q. H.; Zhang, W. H.; Zhou, G. Y.; Zhang, D.; Song, C. L.; He, K.; Ji, S. H.; Chen, X.; Gu, L.; Wang, L. L.; Ma, X. C.; Xue, Q. K. Interface-enhanced high-temperature superconductivity in single-unit-cell $FeTe_{1-x}Se_x$ films on $SrTiO_3$. *Phys. Rev. B* **2015**, *91*, 220503.
(32) Han, Y.; Li, W. Y.; Cao, L. X.; Wang, X. Y.; Xu, B.; Zhao, B. R.; Guo, Y. Q.; Yang, J. L. Superconductivity in Iron Telluride Thin Films under Tensile Stress. *Phys. Rev. Lett.* **2010**, *104*, 017003.
(33) Lee, S. H.; Zhu, Y.; Wang, Y.; Miao, L.; Pillsbury, T.; Yi, H.; Kempinger, S.; Hu, J.; Heikes, C. A.; Quarterman, P.; Ratcliff, W.; Borchers, J. A.; Zhang, H.; Ke, X.; Graf, D.; Alem, N.; Chang, C.-Z.; Samarth, N.; Mao, Z. Spin Scattering and Noncollinear Spin Structure-Induced Intrinsic Anomalous Hall Effect in Antiferromagnetic Topological Insulator $MnBi_2Te_4$. *Phys. Rev. Research* **2019**, *1*, 012011.
(34) Yan, J. Q.; Zhang, Q.; Heitmann, T.; Huang, Z. L.; Chen, K. Y.; Cheng, J. G.; Wu, W. D.; Vaknin, D.; Sales, B. C.; McQueeney, R. J. Crystal growth and magnetic structure of $MnBi_2Te_4$. *Phys. Rev. Mater.* **2019**, *3*, 064202.
(35) Dai, P. C. Antiferromagnetic order and spin dynamics in iron-based superconductors. *Rev. Mod. Phys.* **2015**, *87*, 855−896.
(36) Enayat, M.; Sun, Z. X.; Singh, U. R.; Aluru, R.; Schmaus, S.; Yaresko, A.; Liu, Y.; Lin, C. T.; Tsurkan, V.; Loidl, A.; Deisenhofer, J.; Wahl, P. Real-space imaging of the atomic-scale magnetic structure of Fe1+yTe. *Science* **2014**, *345*, 653−656.
(37) Bao, W.; Qiu, Y.; Huang, Q.; Green, M. A.; Zajdel, P.; Fitzsimmons, M. R.; Zhernenkov, M.; Chang, S.; Fang, M. H.; Qian, B.; Vehstedt, E. K.; Yang, J. H.; Pham, H. M.; Spinu, L.; Mao, Z. Q. Tunable ($\delta\pi$, $\delta\pi$)-Type Antiferromagnetic Order in α-Fe(Te,Se) Superconductors. *Phys. Rev. Lett.* **2009**, *102*, 247001.
(38) Li, S. L.; de la Cruz, C.; Huang, Q.; Chen, Y.; Lynn, J. W.; Hu, J. P.; Huang, Y. L.; Hsu, F. C.; Yeh, K. W.; Wu, M. K.; Dai, P. C. First-order magnetic and structural phase transitions in $Fe_{1+y}Se_xTe_{1-x}$. *Phys. Rev. B* **2009**, *79*, 054503.
(39) Manna, S.; Kamlapure, A.; Cornils, L.; Hanke, T.; Hedegaard, E. M. J.; Bremholm, M.; Iversen, B. B.; Hofmann, P.; Wiebe, J.; Wiesendanger, R. Interfacial superconductivity in a bi-collinear antiferromagnetically ordered FeTe monolayer on a topological insulator. *Nat. Commun.* **2017**, *8*, 14074.
(40) Yi, H.; Hu, L.-H.; Zhao, Y.-F.; Zhou, L.-J.; Yan, Z.-J.; Zhang, R.; Yuan, W.; Wang, Z.; Wang, K.; Hickey, D. R.; Richardella, A. R.; Singleton, J.; Winter, L. E.; Wu, X.; Chan, M. H. W.; Samarth, N.; Liu, C.-X.; Chang, C.-Z. Dirac-fermion-assisted interfacial superconductivity in epitaxial topological-insulator/iron-chalcogenide heterostructures. *Nat. Commun.* **2023**, *14*, 7119.
(41) Ovchinnikov, D.; Huang, X.; Lin, Z.; Fei, Z.; Cai, J.; Song, T.; He, M.; Jiang, Q.; Wang, C.; Li, H.; Wang, Y.; Wu, Y.; Xiao, D.; Chu, J. H.; Yan, J.; Chang, C. Z.; Cui, Y. T.; Xu, X. Intertwined Topological and Magnetic Orders in Atomically Thin Chern Insulator $MnBi_2Te_4$. *Nano Lett.* **2021**, *21*, 2544−2550.
(42) Yang, S.; Xu, X.; Zhu, Y.; Niu, R.; Xu, C.; Peng, Y.; Cheng, X.; Jia, X.; Huang, Y.; Xu, X.; Lu, J.; Ye, Y. Odd-Even Layer-Number Effect and Layer-Dependent Magnetic Phase Diagrams in $MnBi_2Te_4$. *Phys. Rev. X* **2021**, *11*, 011003.
(43) Wang, J.; DaSilva, A. M.; Chang, C. Z.; He, K.; Jain, J. K.; Samarth, N.; Ma, X. C.; Xue, Q. K.; Chan, M. H. W. Evidence for Electron-Electron Interaction in Topological Insulator Thin Films. *Phys. Rev. B* **2011**, *83*, 245438.
(44) Liu, M. H.; Chang, C. Z.; Zhang, Z. C.; Zhang, Y.; Ruan, W.; He, K.; Wang, L. L.; Chen, X.; Jia, J. F.; Zhang, S. C.; Xue, Q. K.; Ma, X. C.; Wang, Y. Y. Electron Interaction-Driven Insulating Ground State in Bi_2Se_3 Topological Insulators in the Two-Dimensional Limit. *Phys. Rev. B* **2011**, *83*, 165440.
(45) Huang, Z. L.; Du, M. H.; Yan, J. Q.; Wu, W. D. Native defects in antiferromagnetic topological insulator MnBi2Te4. *Phys. Rev. Mater.* **2020**, *4*, 121202.
(46) Dynes, R. C.; Narayanamurti, V.; Garno, J. P. Direct Measurement of Quasiparticle-Lifetime Broadening in a Strong-Coupled Superconductor. *Phys. Rev. Lett.* **1978**, *41*, 1509−1512.

https://doi.org/10.1021/acs.nanolett.4c01407
Nano Lett. 2024, 24, 7962−7971

(47) Qi, X. L.; Hughes, T. L.; Zhang, S. C. Chiral Topological Superconductor from the Quantum Hall State. *Phys. Rev. B* **2010**, *82*, 184516.
(48) Kayyalha, M.; Xiao, D.; Zhang, R. X.; Shin, J.; Jiang, J.; Wang, F.; Zhao, Y. F.; Xiao, R.; Zhang, L.; Fijalkowski, K. M.; Mandal, P.; Winnerlein, M.; Gould, C.; Li, Q.; Molenkamp, L. W.; Chan, M. H. W.; Samarth, N.; Chang, C. Z. Absence of evidence for chiral Majorana modes in quantum anomalous Hall-superconductor devices. *Science* **2020**, *367*, 64−67.
(49) Wang, J.; Zhou, Q.; Lian, B.; Zhang, S. C. Chiral Topological Superconductor and Half-Integer Conductance Plateau from Quantum Anomalous Hall Plateau Transition. *Phys. Rev. B* **2015**, *92*, 064520.

https://doi.org/10.1021/acs.nanolett.4c01407
Nano Lett. 2024, 24, 7962−7971